



On the Nature of Propagating Intensity Disturbances in Polar Plumes during the 2017 Total Solar Eclipse

Kyung-Suk Cho^{1,2} , Il-Hyun Cho³ , Maria S. Madjarska^{4,5} , Valery M. Nakariakov^{3,6} , Heesu Yang¹ , Seonghwan Choi¹ , Eun-Kyung Lim¹ , Kyung-Sun Lee⁴, Jung-Jun Seough¹, Jaeok Lee¹, and Yeon-Han Kim¹

¹ Space Science Division, Korea Astronomy and Space Science Institute, Daejeon 305-348, Republic of Korea; kscho@kasi.re.kr

² Department of Astronomy and Space Science, University of Science and Technology, Daejeon 305-348, Republic of Korea

³ School of Space Research, Kyung Hee University, Yongin, 17104, Republic of Korea

⁴ Astronomy Program, Department of Physics and Astronomy, Seoul National University, Seoul 151-742, Republic of Korea

⁵ Max Planck Institute for Solar System Research, Justus-von-Liebig-Weg 3, D-37077, Göttingen, Germany

⁶ University of Warwick, Coventry, CV4 7AL, UK

Received 2020 October 15; revised 2021 January 22; accepted 2021 January 24; published 2021 March 18

Abstract

The propagating intensity disturbances (PIDs) in plumes are still poorly understood, and their identity (magnetoacoustic waves or flows) remains an open question. We investigate PIDs in five plumes located in the northern polar coronal hole observed during the 2017 total solar eclipse. Three plumes are associated with coronal bright points, jets, and macrospicules at their base (active plumes), and the other two plumes are not (quiet plumes). The electron temperature at the base of the plumes is obtained from the filter ratio of images taken with the X-ray Telescope on board Hinode and the passband ratio around 400 nm from an eclipse instrument, the Diagnostic Coronagraph Experiment. The phase speed (v_r), frequency (ω), and wavenumber (k) of the PIDs in the plumes are obtained by applying a Fourier transformation to the spacetime ($r-t$ plane) plots in images taken with the Atmospheric Imaging Assembly (AIA) in three different wavelength channels (171, 193, and 211 Å). We found that the PIDs in the higher-temperature AIA channels, 193 and 211 Å, are faster than that of the cooler AIA 171 Å channel. This tendency is more significant for the active plumes than the quiet ones. The observed speed ratio (~ 1.3) between the AIA 171 and 193 Å channels is similar to the theoretical value (1.25) of a slow magnetoacoustic wave. Our results support the idea that PIDs in plumes represent a superposition of slow magnetoacoustic waves and plasma outflows that consist of dense cool flows and hot coronal jets.

Unified Astronomy Thesaurus concepts: Solar coronal waves (1995); Solar coronal plumes (2039); X-ray bright point (1812); Solar eclipses (1489); Fast solar wind (1872); Solar coronal holes (1484); Solar coronal heating (1989)

Supporting material: animation

1. Introduction

Polar plumes are long-lasting, dense, raylike, and relatively bright solar corona structures, usually observed in the extreme UV (EUV), X-ray, and white light. They are magnetically open linear structures extending from the Sun's surface to about $30 R_\odot$ and known to be a source of the fast solar wind (Poletto 2015; Zangrilli & Giordano 2020, and references therein). Raouafi et al. (2008) suggested that low-rate magnetic reconnection is responsible for the formation and sustainability of plumes. Plumes are thought to be associated with coronal bright points (CBPs; Madjarska 2019) that form at the boundaries of supergranulation cells. Several observations support the idea that polar plumes are associated with CBPs, X-ray jets, or EUV jets in the network regions (Raouafi & Stenborg 2014). Wang & Sheeley (1995) suggested that the properties of a few hours' long and hazy plume structure can be adequately explained by the quasi-static upward evaporation of material heated by conduction during magnetic reconnection at the boundary of the supergranular cells. This suggestion was supported by the observations of a particularly bright plume taken with the Solar Heliospheric Observatory/Coronal Diagnostic Spectrometer (SOHO/CDS). Young et al. (1999) investigated a plume above the limb and the plume base visible on the solar disk. They reported that the temperature of the plume above the limb is about 1 MK, and the temperature

remains constant with height. They found a strong brightening lying directly below the plume's main body with a high temperature of 2 MK, i.e., a CBP. They suggested that the footpoint morphology is similar to an emerging bipole in a region of unipolar magnetic flux, which is typical for CBPs (Madjarska 2019).

Due to the open magnetic configuration in polar coronal holes, polar plumes could be waveguides for magnetohydrodynamic (MHD) waves (e.g., Nakariakov 2006; Poletto 2015). The existence of waves in plumes has been demonstrated by observations taken with the UltraViolet Coronagraph Spectrometer (Ofman et al. 1997), Extreme ultraviolet Imaging Telescope (DeForest & Gurman 1998), CDS (Banerjee et al. 2000), Solar Ultraviolet Measurements of Emitted Radiation (Gupta et al. 2012) on board SOHO, and a theoretical model for the propagation of magnetoacoustic waves in polar plumes by Ofman et al. (1999).

Propagating intensity disturbances (PIDs) in plumes have been interpreted as compressible magnetoacoustic waves, as their intensity enhancement coincides with the blueshift of the O V 629 Å line profile taken with CDS (Banerjee et al. 2000). Banerjee et al. (2009) observed intensity oscillations with a period of 10–30 minutes and propagation velocity from 75 to 125 km s^{−1}, depending on the line formation temperature. They concluded that the most likely cause for PIDs is slow magnetoacoustic waves. This conclusion was supported by

Gupta et al. (2012), who reported a detection of simultaneous intensity enhancement and Doppler velocities of PIDs. The observational evidence that favors the interpretation of PIDs in terms of slow magnetoacoustic waves is summarized in Banerjee et al. (2011). Meanwhile, McIntosh et al. (2010) suggested that plumes are associated with high-speed jets that are multithermal and repeat quasiperiodically. Later, Tian et al. (2011) supported this by showing the significant asymmetries of spectral lines observed with the Extreme-ultraviolet Imaging Spectrometer/Hinode. On the other hand, Verwichte et al. (2010) demonstrated that the line asymmetry is fully consistent with the interpretation of PIDs in terms of upward propagating compressive waves. Pucci et al. (2014) concluded that PIDs represent plasma outflows because the expected temperature dependence of the magnetoacoustic wave was not observed. In their data, the apparent speed ($30\text{--}300\text{ km s}^{-1}$) is higher in the low-temperature channel, AIA 171 Å, than in the high-temperature channels, AIA 193 and 211 Å. On the other hand, Krishna Prasad et al. (2011) established the temperature dependence of the apparent phase speed, theoretically predicted for slow magnetoacoustic waves. Moreover, Gupta (2014) found that the dissipation lengths of PIDs are frequency-dependent, which is consistent with the slow wave behavior. A recent analysis of the damping and power spectra of PIDs in coronal holes, observed with SDO/AIA, links this phenomenon with slow magnetoacoustic waves too (Jiao et al. 2016). In addition, similar wave motions are routinely detected in the legs of coronal loops, and their observed properties are well described by the MHD wave theory (e.g., de Moortel 2009; De Moortel & Nakariakov 2012).

Due to the overlapping of the plume structures with foreground and background emission and the lack of observations with a sufficiently high spatial resolution, the polar plume's triggering mechanism is still not well understood. For this reason, the observations of the footpoints of the polar plumes are vital, as they can give a clear connection from the bipole emergence through the H α /EUV/X-ray jets to the polar plumes. In this study, we investigate plumes in a polar coronal hole to inspect PIDs and their relationship with activities at the base of the plumes. For this, we analyze polar plumes that are found in an image taken at the 2017 total solar eclipse (TSE) using the Diagnostic Coronagraph Experiment (DICE), Hinode X-ray Telescope (XRT), SDO/AIA, and SOHO Large Angle and Spectrometric Coronagraph Experiment (LASCO) images. We divide the plumes into active and quiet ones and derive the wavenumber and frequency of PIDs using the Fourier component analysis to investigate a phase speed dependency on the temperature.

The following Section describes observation and data processing. In Section 3, we present spacetime plots of plumes and dispersion relations of the propagation in the plumes. Finally, we summarize and discuss our results in Section 4.

2. Observations and Data Processing

The observation targets are plumes observed at the north polar limb during the TSE on 2017 August 21 at Jackson Hole, Wyoming. The obtained data from the eclipse observation are white-light (WL) images and narrowband polarization images around 400 nm. The WL images were taken using a simple camera system consisting of a Canon 400 mm lens with a 2X extender. During the TSE, we took WL images with different exposure times from 0.15 ms to 0.25 s to acquire features from

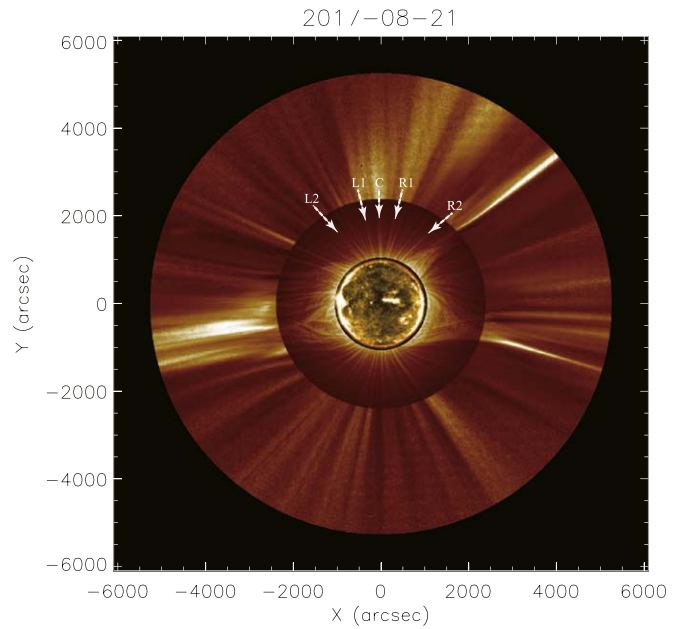


Figure 1. Composite image of LASCO C2 ($R > 2.5 R_{\odot}$), the WL image ($1.1 R_{\odot} \leq R \leq 2.5 R_{\odot}$), and AIA 171 Å ($R < 1.10 R_{\odot}$). The WL image is produced using the WL images taken by a Canon 400 mm camera during the total eclipse of 2017 August 21 (17:35–17:37 UT), and AIA 171 Å was obtained at 17:45 UT. The LASCO C2 image is the mean intensity between 16:00 and 20:00 UT. Arrows denote the plumes in the north coronal hole for this study.

the chromosphere to the outer corona ($> 3 R_{\odot}$). After the image alignment and rotation, we applied the multiscale Gaussian normalization method (Morgan & Druckmüller 2014) to the WL images. This processing dramatically enhances the faint plume intensity signal at a high altitude. The pixel resolution of the WL images is about $1''.03$. Narrowband images were taken using the DICE consisting of an optical assembly, a filter wheel, a polarizer unit, and a CCD camera. Since the temperature determines the shape of the coronal spectrum (Thompson-scattered photospheric light), we used the polarization intensity ratio at the temperature-sensitive wavelengths at 393.9 and 402.5 nm and determined the coronal temperature by applying the method suggested by Cram (1976). The pixel size of the polarization data is about $12''.7$, and we used 3 by 3 data binning of stacked images after aligning the images for specific filters and polarization angles to obtain a temperature map. The temperature measurements using the passband ratio imaging were conducted during the TSE (Reginald et al. 2017) and Balloon mission (Gopalswamy et al. 2020). A more detailed description of the DICE instrument and data reduction can be found in Cho et al. (2020). First, from the DICE observations, we identified regions of enhanced emission associated with CBPs, and their temperature was first determined. To verify the CBPs and temperature at the base of the plumes, we also checked the data taken with the XRT (Golub et al. 2007) on board Hinode (Kosugi et al. 2007) during the eclipse time. It was noted that the temperature structures in the DICE data are generally similar to those in the XRT images, but CBPs could not be seen in the DICE data due to occulting the solar disk by the Moon. We used level 1 data of XRT processed by xrt_prep.pro. The pixel resolution of the XRT images is about $1''$. By taking a full-Sun image observed at 16:43 UT, we calculated the electron temperature by applying the xrt_teem.pro to the “Al-poly” and “Al-mesh” filter data pair, which is sensitive for

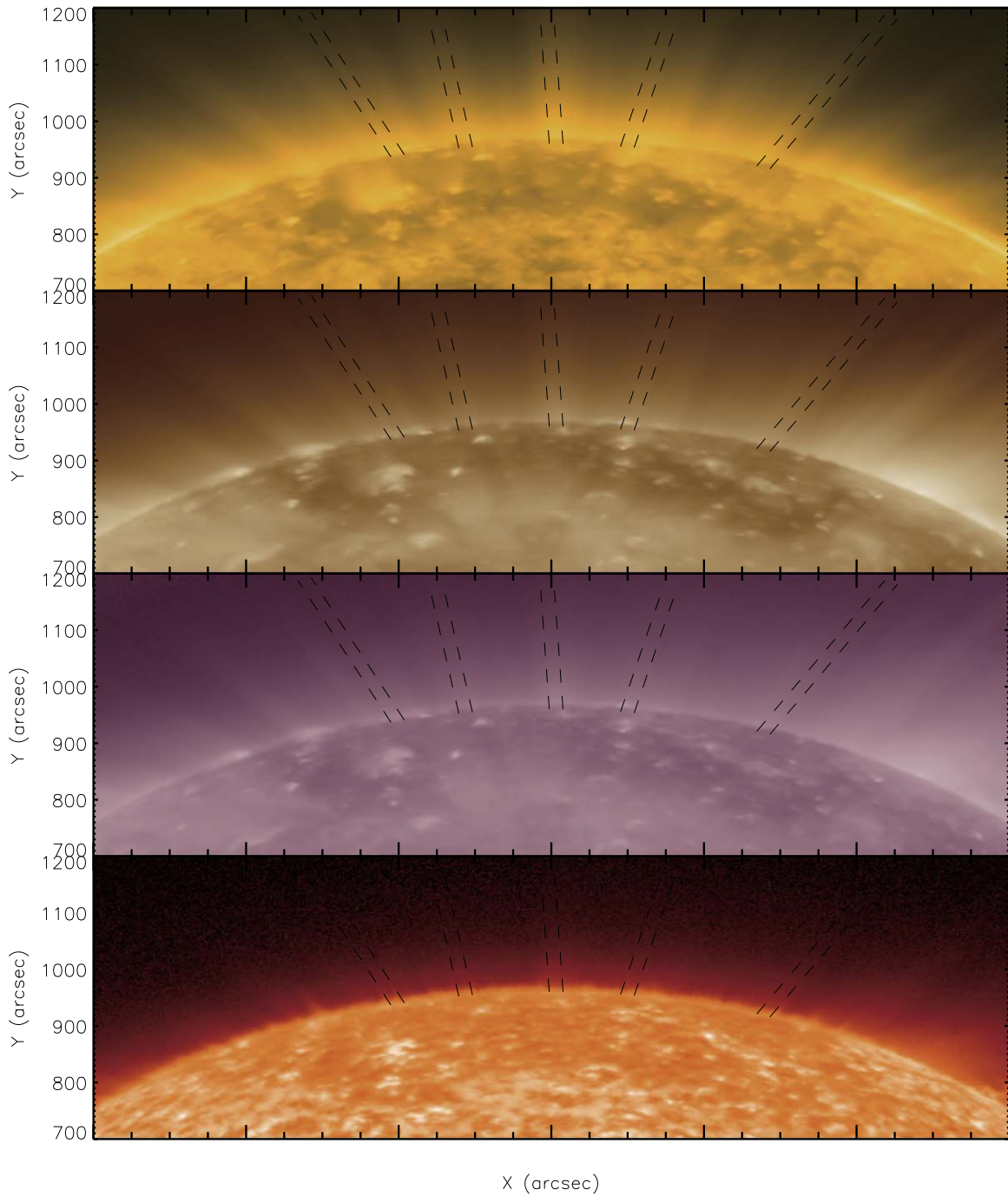


Figure 2. Averaged SDO/AIA images between 16:00 and 17:40 UT to enhance the structure of plumes denoted by arrows in Figure 1. The AIA 171, 193, 211, and 304 Å channels are plotted in the panels from top to bottom. Dotted slots along the plumes are used to inspect activities at the bottom of the plumes and trace flows in the plumes marked with arrows in Figure 1. See the accompanying animation from 16:00 to 17:40 UT, which shows outflows and jets in the plumes and recurrent spicules and macrospicules in the base of the plumes. An animation of this figure is available in the online journal.

(An animation of this figure is available.)

Table 1
Activities of the Plumes

	L2	L1	C	R1	R2
Jet occurrence	No	Yes	Yes	Yes	No
Macrospicule	Quiet	Active	Active	Active	Quiet
Footpoint temp.	Low	High	High	High	Low
Plume activity	Quiet	Active	Active	Active	Quiet

temperatures from $\log T = 5.5$ up to $\log T = 6.3$ (Narukage et al. 2014).

We also used SOHO (Domingo et al. 1995)/LASCO C2 (Brueckner et al. 1995) and SDO (Pesnell et al. 2012)/AIA (Lemen et al. 2012) data to inspect the off-limb plume structure and dynamics. The level 0.5 data of LASCO C2 from 16:00 to 20:00 UT were used to produce an imaging data cube. We normalized the data set in a temporal direction by subtracting a

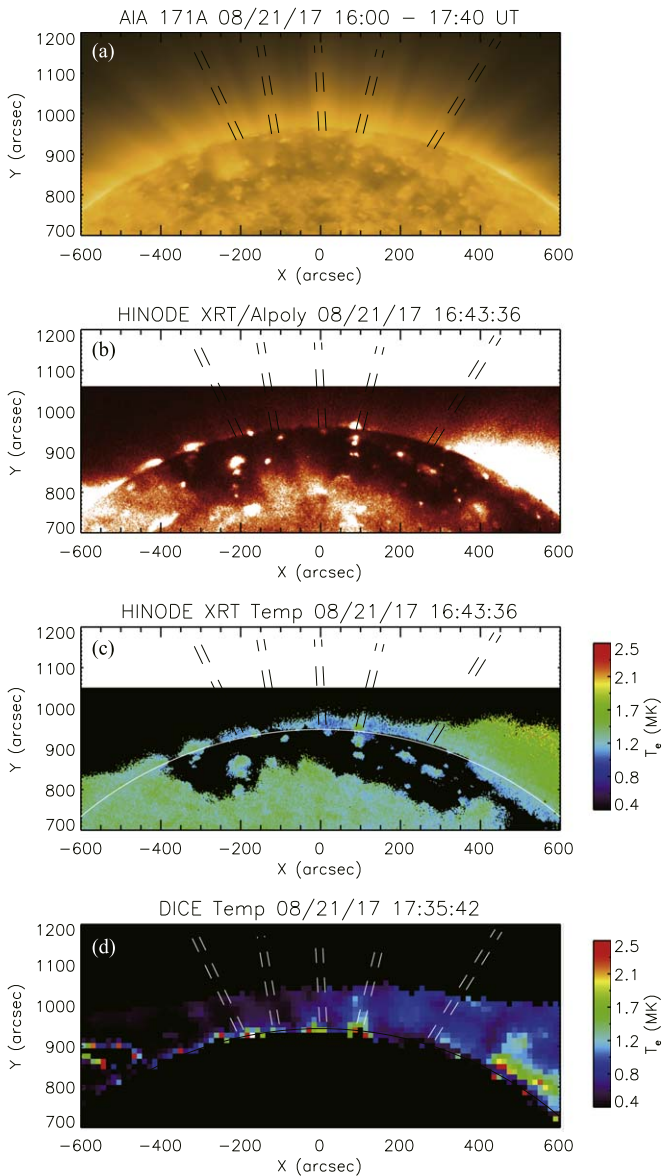


Figure 3. The EUV and X-ray images together with coronal temperature maps from Hinode/XRT and 2017 TSE experiment, DICE. (a) AIA 171 Å image taken at 17:36 UT. (b) Hinode XRT/Al-poly image before the eclipse. (c) Temperature map calculated by the ratio method using Al-mesh and Al-poly data. (d) Temperature map calculated by the ratio method using polarized brightness images taken at 3934 and 4025 Å. The dashed slots denote the same locations as in Figure 2.

background image, including the F-coronal and instrument stray light. We calculated all pixel median values between 2.2 and $5.8 R_{\odot}$ in a temporal direction. We subtracted this value from the data set and divided by the corresponding standard absolute deviation. We took an averaged image from the processed data cube after removing the blinking due to frame-to-frame variation in exposure time and spikes (stars) in the data. The AIA 171, 193, 211, and 304 Å data with a 12 s time cadence and $0''.6$ pixel $^{-1}$ scale were used to inspect the dynamics of the plume footpoints within the range from 1 to $1.26 R_{\odot}$. To produce a spacetime image $I(r, t)$, we defined slit cuts along the plume lengths in the AIA data. The position of a slit was determined by a linear fitting from the visually determined locations. Thus, the inclined distance of the slits represents the distance from the solar surface. The intensities

along the slits and time are used to investigate the plume dynamics. For a given distance, we divided the original time series by its temporal average and took the first-order time difference that is obtained by subtracting the previous intensity from the current one. Then we applied a median filter with a spatiotemporal window ($3 \text{ minutes} \times 1.5 \text{ Mm}$ size) to eliminate the noise. In the case of AIA 304 Å, the spacetime image is subtracted and then divided by the temporal mean and standard deviation to remove the background (Morgan et al. 2006).

From the AIA slit images, we derived the properties of localized moving features in the plumes using Fourier transformation. To calculate the propagation speed, we applied the Fourier transformation to the spacetime image. The propagating feature in $I(r, t)$ appears in the Fourier power ($|F(k_r, \omega)|^2$), and its phase speed could be defined as $(-\omega/k_r)$. Hence, a positively propagating feature in $I(r, t)$ appears as a prominent power in the second and fourth quadrants in the Fourier space (e.g., the Appendix in DeForest et al. 2014). We set a slit along the plumes in the AIA channels to track the PIDs and generate an $I(r, t)$ image that contains both the temporal and spatial information of the propagation. A Fourier transformation is applied to the $I(r, t)$ image to obtain its conjugate (k_r, ω) plane. This results in the observational dispersion relationship for the frequency (ω) as a function of wavenumber (k_r). Since moving features with a speed in the $I(r, t)$ plane are transformed to features lying along a diagonal line in the (k_r, ω) plane, we can derive a particular speed of the propagation features by measuring the slope (ω/k_r) of the diagonal line (e.g., Figure 1 in DeForest et al. 2014).

3. Results

For tracing the plumes to the solar surface, we used the SDO/AIA, SOHO/LASCO C2, and eclipse data. Figure 1 shows the WL eclipse image that is composed of SDO/AIA 171 Å in the lower corona and LASCO C2 images in the upper corona. The polar coronal hole in the northern hemisphere contains dense and relatively bright plumes extending from the solar surface to about $5.5 R_{\odot}$. We used the eclipse image that fills a gap between the lower corona ($< 1.2 R_{\odot}$) and the upper corona ($2.5 R_{\odot} \leq R \leq 5.5 R_{\odot}$). In this study, we selected the plumes whose connection from the higher corona to the surface is clear and then marked them with arrows and labels, as shown in Figure 1. It is noted from the eclipse and LASCO images that the plumes (L1, C, and R1) in the middle are brighter and more extended into the higher corona than the others (L2 and R2). The plumes L1, C, and R1 correspond to the coronal fine structures 3, 2, and 1, respectively, in Figure 1 of Hanaoka et al. (2018).

We inspected the location where these plumes are rooted in the AIA images to study the physical properties of the plasma at the plume footpoints. Figure 2 shows the averaged intensity maps of the AIA 171, 193, 211, and 304 Å channels (top to bottom). These maps are obtained from the AIA images with 12 s cadence during 100 minutes from 16:00 to 17:40 UT. Except for the AIA 304 Å channel, plume structures are seen in all AIA channels. The plumes in the AIA 171 Å channel (maximum response temperature $T_e \sim 0.7 \times 10^6 \text{ K}$ from the Fe IX line; O'Dwyer et al. 2010) are brighter and denser than those seen in the AIA 191 and 211 Å channels. The plumes are also detected in the high-temperature channels of AIA 193 ($0.7 \times 10^6 \text{ K} \leq T_e \leq 1.6 \times 10^6 \text{ K}$) and 211 Å ($T_e \sim 1.1 \times 10^6$ and $1.4 \times 10^6 \text{ K}$ for the Fe X and Fe XI lines, respectively). In

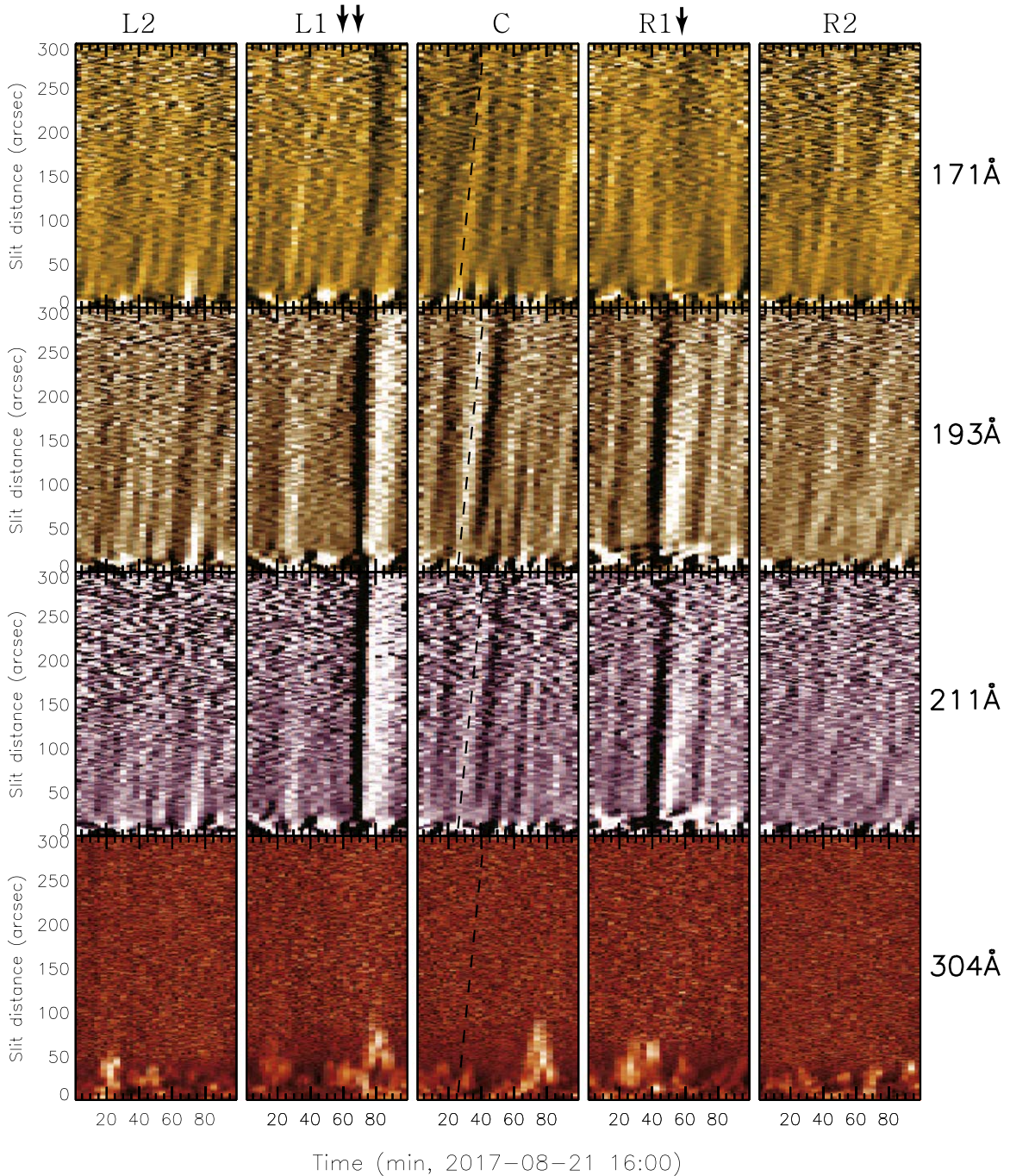


Figure 4. Spacetime plots of the detrended AIA 171, 193, 211, and 304 Å images (top to bottom). From left to right, the spacetime plots are displayed for the regions of L2, L1, C, R1, and R2 in Figure 3(b). Dashed lines denote an example of strips, and arrows indicate AIAC strips missing in AIAH, and vice versa (see text).

this study, we will refer to the high-temperature channels AIA 193 and 211 Å as AIAH and the low-temperature channel AIA 171 Å as AIAC. As it can be noted from Figure 2, cool and hot plasma coexists in plumes. From the animation of Figure 2, we identified apparent outflows in the plumes in AIAH and AIAC and recurrent spicules and macrospicules in the base of the plumes from the 304 Å channel animation. In AIAH, EUV jets are identified in the plumes L1, C, and R1, which have CBPs in their footpoints and extend to the higher corona with brighter structures seen in the LASCO C2 field of view, as shown in Figure 1. We summarized the plumes' activities in Table 1.

Based on the multisite WL observations during the 2017 TSE, Hanaoka et al. (2018) reported that these plumes are

associated with the coronal (eclipse) jets, while the L2 plume is not accompanied by WL jets seen during the eclipse. According to their study, the jets associated with the plumes were upwardly ejected with an apparent speed of about 450 km s^{-1} beyond $2 R_{\odot}$. The R2 plume that has no jets, macrospicules, and a CBP is not studied in their work.

As suggested by Wang & Sheeley (1995), the plumes' hazy structures in high-temperature imaging channels may be due to quasi-static upward evaporation heated by thermal conduction following magnetic reconnection. This suggestion led us to inspect the temperature structure at the base of the plumes. The temperature was estimated from the Hinode/XRT and DICE data by applying the methods described in the previous section.

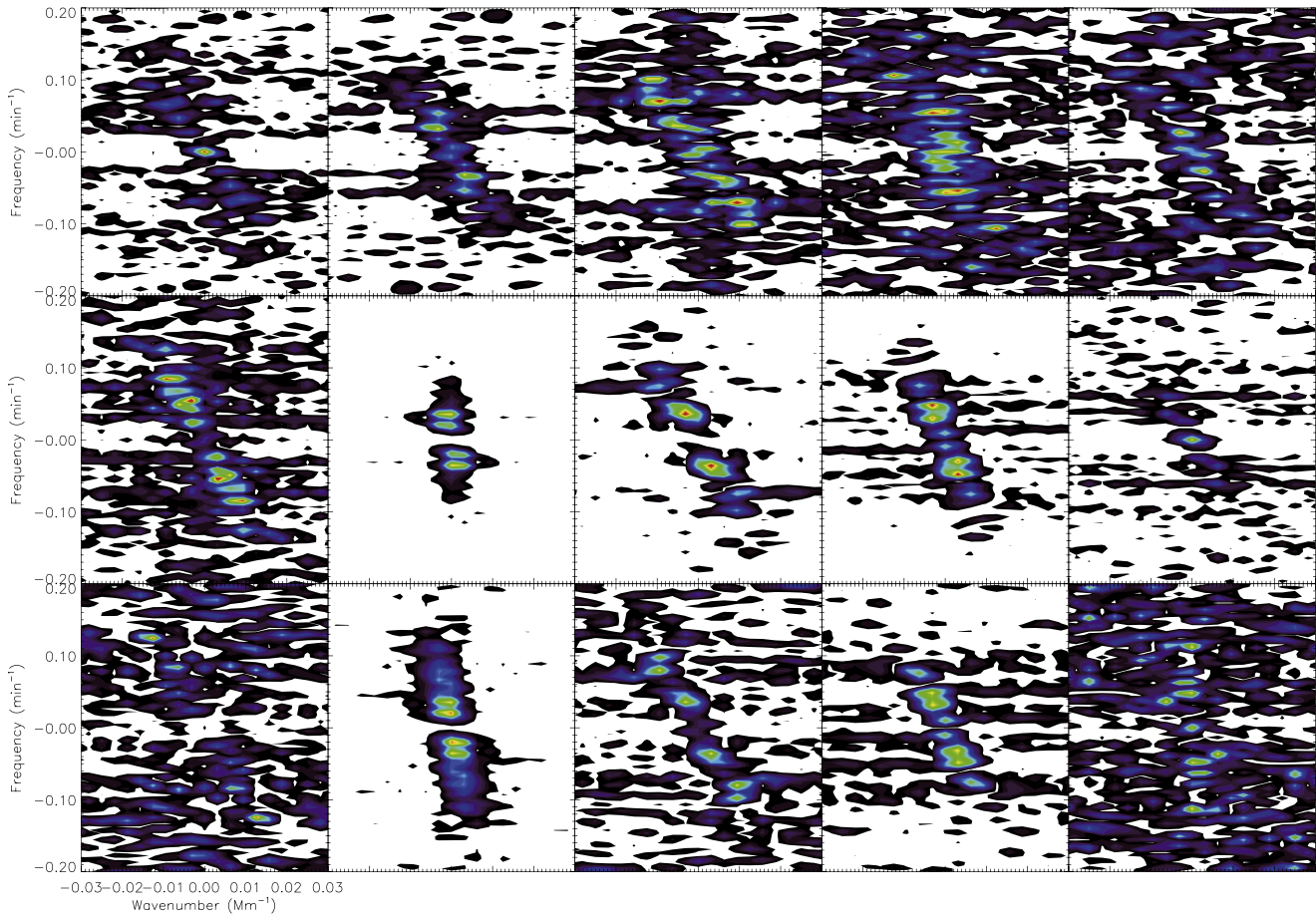


Figure 5. Wavenumber–frequency (k – ω) maps for the five plumes (left to right) and three AIA channels of 171, 193, and 211 Å (top to bottom).

Figure 3 shows EUV and soft X-ray intensity images and temperature maps from XRT and DICE. The XRT image was taken with the “Al-poly” filter. It shows that EUV brightenings at the base of the plumes (L1, C, and R1), are consistent with CBPs, and the temperature structures from XRT and DICE look similar to each other. It reveals that the plumes (L1, C, and R1) that have jets are associated with CBPs in their bases. Their temperature ranges between 1 and 1.5 MK (Figures 3(c) and (d)). The other plumes, L2 and R2, have no CBPs at their bases, and their temperatures are not significantly high.

Flows of hot and cool plasma in the plumes were investigated by using spacetime plots along the plumes, tracing them from the limb. By using the method described in Section 2, we produced spacetime plots over the dashed bars in Figure 2, as shown in Figure 4. In Figure 4, the oblique alternating bright and dark stripes represent the intensity disturbances that propagate upwardly along the plumes. The strips in AIAH look similar and are more prominent in AIA 193 Å due to a lower signal-to-noise ratio of AIA 211 Å. Most of the strips in AIAH coincide with those in AIAH. However, we find that some faint AIAH strips between 17:00 and 17:10 UT are missing in AIAH, as denoted by arrows in the panel of the L1 plume in Figure 4, and vice versa (e.g., the jet in AIAH at 17:00 UT, as marked by an arrow on the panel of the R1 plume). In the plumes (L1, C, and R1) we find macrospicules that rise to up to 50'' and later fall back (AIA 304 panels of Figure 4). There is a difference between the jet and the macrospicule activities. For instance, the bright jet (black dashed line) in the C plume is associated with a weak

macrospicule, while the big macrospicule at $\sim 17:00$ UT is associated with a weak PID in AIAH and AIAC. The one-to-one connection between the macrospicules and the jets has ambiguity. It is quite clear for the L1 and R1 plumes but not for the C plume.

Macrospicules in plumes C ($\sim 17:10$ UT) and L1 ($\sim 17:20$ UT) coincide with jets. However, the jet at $\sim 17:00$ UT in plume R1 occurs after the rising of the macrospicule ($\sim 16:20$ UT). It is likely that the macrospicules are related to the CBPs in general.

As marked with the black dashed line in Figure 4, the inclination of a strip for the time axis can be used to estimate the individual strip speed. Since we are interested in the statistics of the PID speed at the different channels of AIA, we performed a Fourier transformation to the spacetime data and obtained a dispersion relation, as shown in Figure 5. The Fourier transformation localizes moving features, and the features with speed in the spacetime $I(r, t)$ plane are transformed to features lying along the diagonal line in the dispersion (k_r, ω) plane. Nonmoving and quasi-stationary features exist at low ω , and the noise sources are distributed isotropically.

To obtain the PID general properties, we obtained the mean Fourier powers of the intensity disturbances in all plumes for the different AIA channels. Figure 6 shows the dispersion relationships of all plumes in the various filters in which the power is enhanced and the noise is reduced. To obtain an average speed of propagating packets with different wavenumber and frequency, we set a diagonal dashed line laid along the features

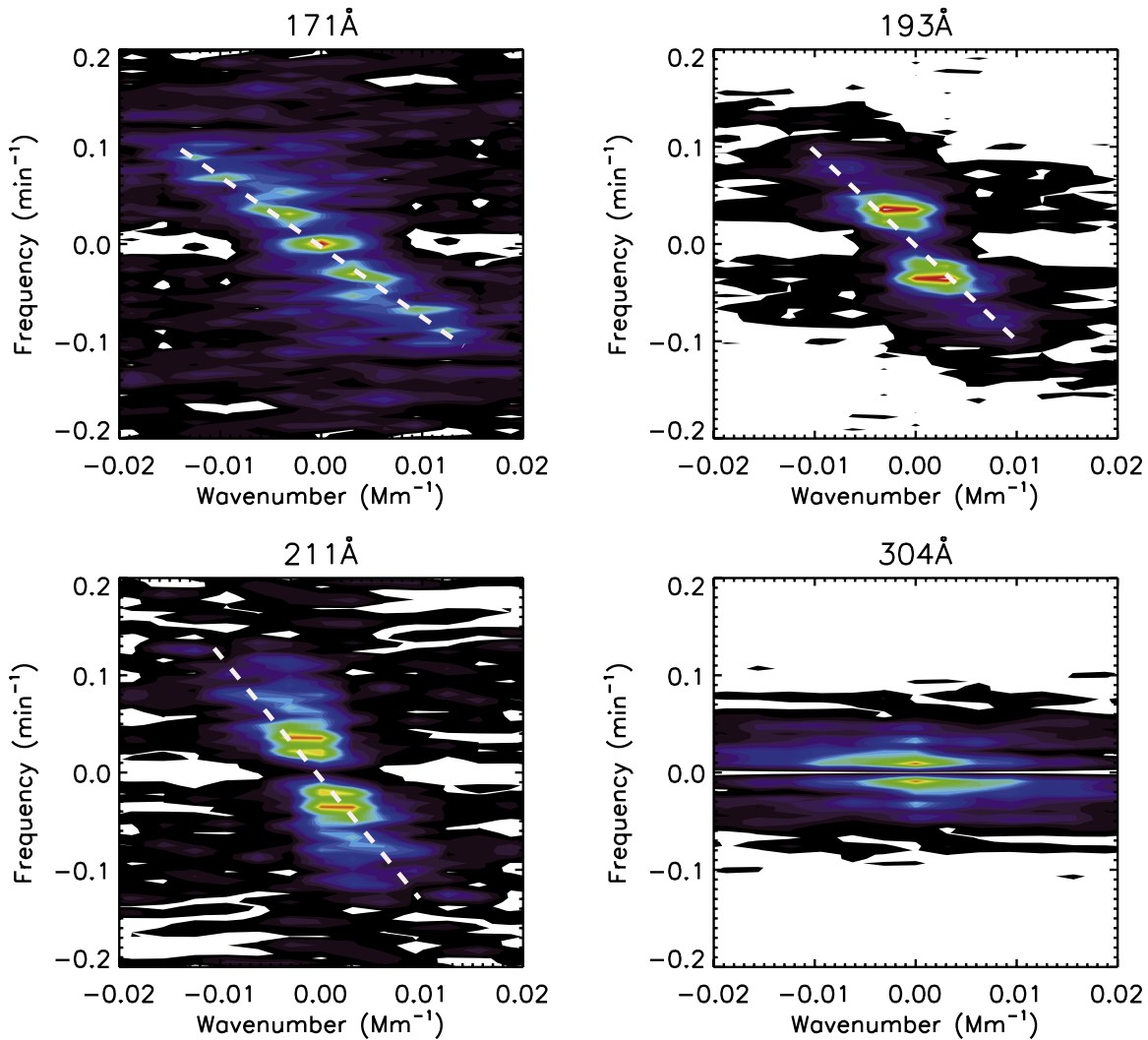


Figure 6. Averaged wavenumber–frequency (k – ω) maps for all plumes in the AIA 171, 193, 211, and 304 Å channels for both groups I and II. The slope of the diagonal dashed line is used to obtain the propagation speed.

as shown in Figure 6 and obtained the propagation speed ($v_r = -\omega/k_r$) from the slope of the diagonal line. When we visually set the line that passes through zero ω and k_r , we did not use the peaks of the power of the plumes located at a small wavenumber and low frequency because they can be related to the jets. In other words, we determined the velocity of the PIDs by considering the features in a high frequency (10–20 minute periods) rather than a low frequency (20–30 minute periods), as in the previous reports by DeForest & Gurman (1998) and Banerjee et al. (2000). For example, $\sim 166 \text{ km s}^{-1}$ in AIA 193 is calculated from a wavenumber of -0.01 Mm^{-1} (wavelength of 100 Mm) and frequency of 0.1 min^{-1} (period of 10 minutes), as shown in the upper right panel of Figure 6. For the different AIA channels, the disturbance speeds (v_r) are not the same but increase as the temperature increases. In the cooler channel (AIA 171 Å), the speed is about 120 km s^{-1} . The wavenumber (k) is shorter than $\sim 66 \text{ Mm}$, and its frequency (ω) is longer than 10 minutes. In comparison to the cool channel, the wave speeds in hot channels are faster, and their wavelengths ($\sim 142 \text{ Mm}$) are longer. The wave speeds in the AIA 193 and 211 Å channels are ~ 162 and $\sim 211 \text{ km s}^{-1}$, respectively. The quasi-stationary features that exist at zero ω and k_r in AIA C disappear in AIA H. Our method contains the measurement errors determined from

10 estimations of the speeds for the different channels. The estimated mean speeds are ~ 123 , ~ 172 , and $\sim 232 \text{ km s}^{-1}$, and their standard deviation errors are ± 3 , ± 6 , and $\pm 24 \text{ km s}^{-1}$ for 171, 193, and 211 Å, respectively.

We classified the plumes into two groups: active (L1, C, and R1) and quiet (L2 and R2) plumes. We added the Fourier power for the active (group I: L1, C, and R1) and quiet (group II: L2 and R2) plumes and investigated their dispersion relations in the AIA 171 and 193 Å channels. Figure 7 shows the relationship between the two groups in the low and high AIA temperature channels, AIA C and AIA H. In AIA C, the wavenumber and frequency of both groups have a similar trend, but the speed of group I ($\sim 130 \text{ km s}^{-1}$) is higher than that of group II ($\sim 116 \text{ km s}^{-1}$). However, the wavenumber and frequency in AIA 193 Å are different for groups I and II. The power of AIA 193 Å of group I is concentrated at a low frequency (~ 30 minutes) and wavenumber, while that of group II has a broad range of frequencies and wavenumbers, as for AIA 171 Å in group I. In AIA H, the speed ($\sim 185 \text{ km s}^{-1}$) of group I is higher than the speed of group II ($\sim 152 \text{ km s}^{-1}$).

The PIDs are detected not only in plumes but also in interplume regions (e.g., Gupta et al. 2010). Thus, we also

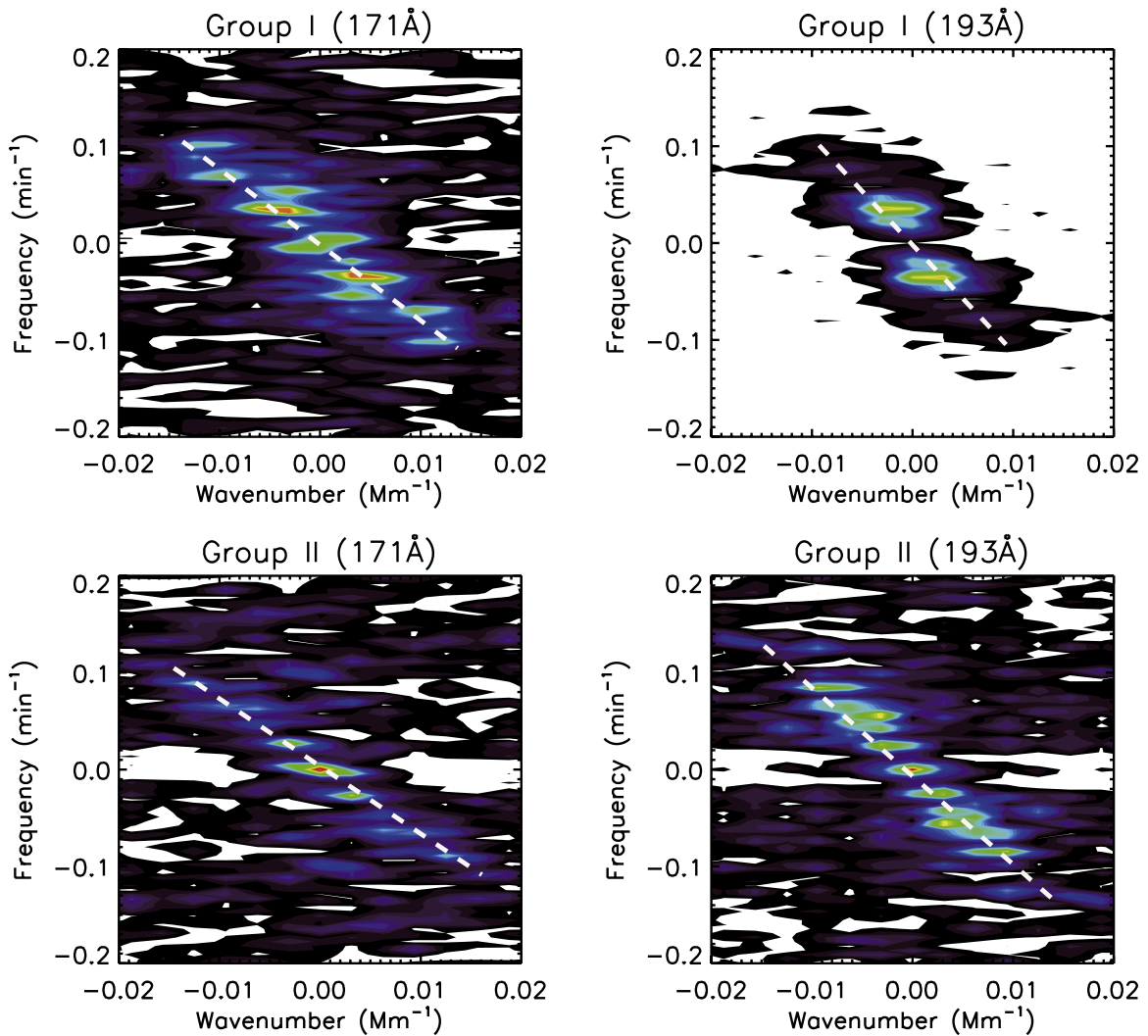


Figure 7. Averaged wavenumber–frequency (k – ω) maps of AIA 171 and 193 Å for plumes with active (upper panels) and quiet (lower panels) footpoints. The slope of the diagonal dashed line is used to obtain a propagation speed.

checked whether PIDs in the interplume regions have a speed–temperature dependency by applying the same method as for PIDs in plume regions. As shown in Figure 8, we took three interplume strips as far as possible from the plumes and then inspected the PIDs and derived their Fourier powers for the different channels. As a result, we cannot identify any clear signature of speed dependency on the temperature from PIDs in the interplume regions. This may be due to the low signal-to-noise ratio because of the low intensity in the interplume regions, especially in the AIAH channels. Other possibilities are thermal imbalance (e.g., Zavershinskii et al. 2019) and steady upflows, which are a property of the equilibrium (e.g., Cho et al. 2020) in the interplume regions and could affect the apparent phase speed of slow waves. It is also noteworthy that the slow waves seen in the structures of different temperatures propagate along different paths in the interplume regions.

4. Summary and Discussion

Five plumes in the polar coronal hole in the northern hemisphere observed during the TSE of 2017 have been investigated using the LASCO C2, SDO/AIA, Hinode/XRT, and DICE data. The plumes were traced back from the high corona ($\sim 5.5 R_{\odot}$ in the LASCO C2 field of view) to the

chromosphere (AIA 304 Å), and the footpoints of the plumes were investigated. We applied 2D Fourier transformation to the spacetime plot of the plumes in the AIA 171, 193, and 211 Å channels and obtained an empirical dispersion relation of the PIDs in the plumes. From the dispersion relation, we found that in all analyzed plumes, PIDs show a temperature dependence of their speed (i.e., the AIAH propagation speed is larger than that of AIAC). This tendency is more evident when we added the Fourier power of all plumes in the different channels. The AIAC has broader ranges of frequencies (ω) and wavenumbers (k) than AIAH. The nonmoving features located at zero frequency and zero wavenumbers in AIAC disappear in AIAH, in which high-power signals are located in the lower frequency and wavenumber.

The quasiperiodic intensity change in Figure 4 is similar to that reported by Tian et al. (2011), who concluded that the intensity change represents outflow (jets) because they did not find an obvious increasing trend in the speed with the increasing temperature. Pucci et al. (2014) reported that the perturbations in AIAC have a higher speed than those in AIAH. They concluded that the radiation variation in the plumes represents outflow material, since their events did not show the temperature dependence that is expected from the

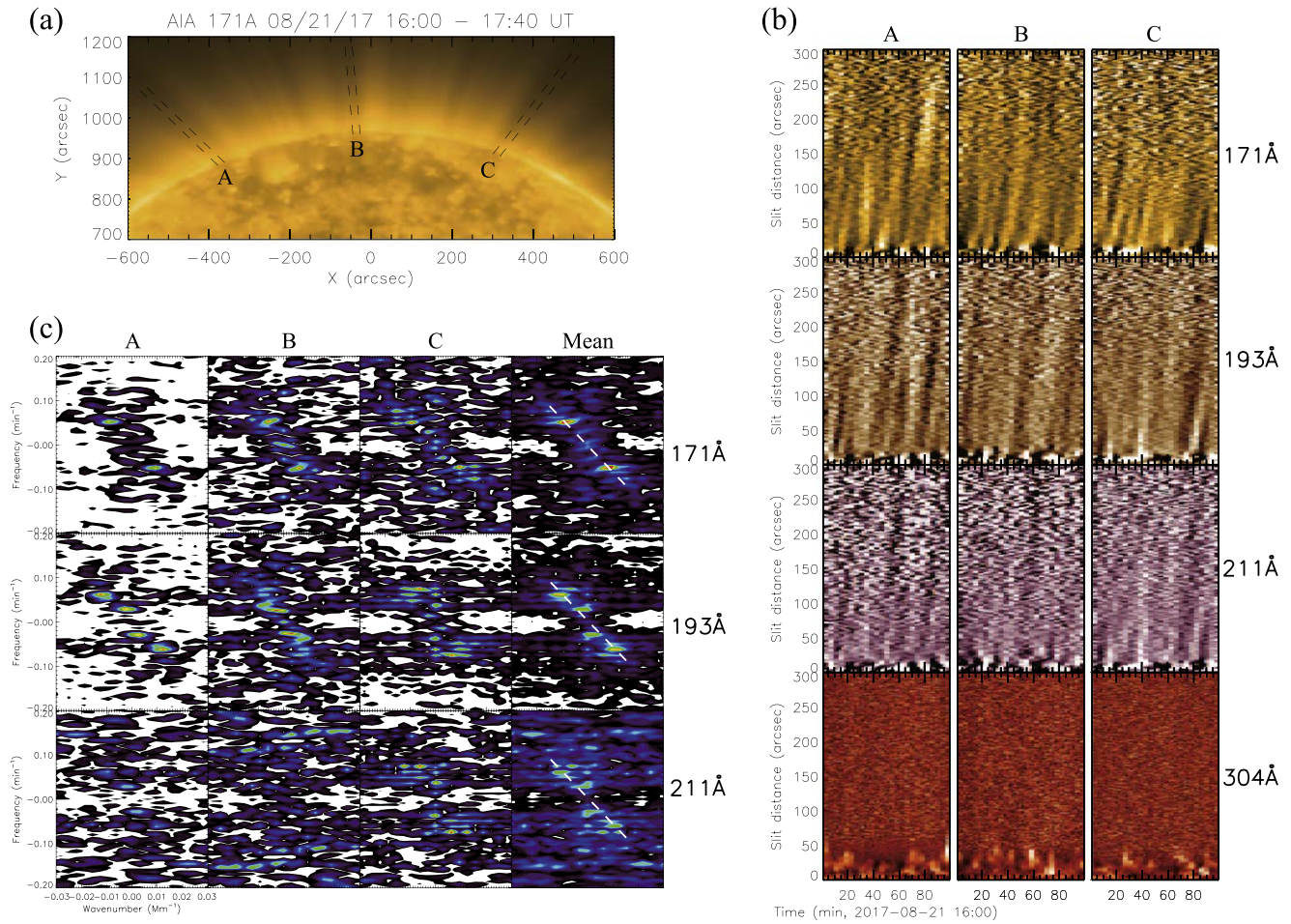


Figure 8. Locations of three interplumes (A, B, and C) and their PID properties. (a) AIA 171 Å image denoted with interplume locations. (b) Spacetime plots of the AIA 171, 193, 211, and 304 Å images (top to bottom). (c) Wavenumber–frequency (k – ω) maps of AIA 171, 193, and 211 Å for the interplumes. The last column of the wavenumber–frequency maps is the mean power map of all interplumes.

magnetoacoustic wave hypothesis. In this study, we have found a temperature dependence of the speed by applying the Fourier transformation. In addition, we found that the observed ratio (~ 1.3) of the speeds in the AIA 171 and 193 Å channels is similar to the expected theoretical value (1.25; Nakariakov 2006; Pucci et al. 2014). These results could be evidence that supports the wave hypothesis.

The events studied here may differ in their properties from those of Pucci et al. (2014), who studied cooler plumes (see Figure 1 in Pucci et al. 2014). Here we have investigated two groups of plumes that have different properties. By measuring temperatures from the XRT and DICE observations, we divided the plumes depending on the existence of the high-temperature CBPs. Active plumes are bright and associated with jets and macrospicules ejected from high-temperature CBPs. These plumes extend as brighter (denser) structures into the higher corona ($\sim 5.5 R_{\odot}$). The quiet plumes are less bright, diffuse, and quasi-stable structures and possibly represent the decay stage of the plume evolution. Propagation speeds of PIDs in active plumes are higher than those of quiet plumes, and this tendency is more significant in AIAH. The active and quiet plumes have different wavenumbers and frequency patterns in AIAH, but their difference is not discernible in AIAC. It is noteworthy mentioning that the active plumes associated with

CBPs may be an early stage of the plume’s evolution (see Del Zanna et al. 2003). The disturbance speed in AIAC is lower than that of AIAH, but the difference is not more significant than active plumes (group I). From the AIAH movie from August 19–23, it is noted that the CBP in the footpoints of quiet plume L2 disappeared and the plume became quieter by the time of the eclipse observations on August 21. The footpoint behavior of R2 could not be inspected because the footpoint of the R2 plume moves behind the limb.

Our results lead us to conclude that the emission intensity variations in the studied plumes represent slow magnetoacoustic waves. However, we cannot rule out the coexistence of plasma outflows with slow waves. The plumes’ flows are likely to consist of cool and dense material from macrospicules and high-temperature jets from CBPs. The flows seen in the low-temperature channels may be plasma flows produced by quasi-static upward evaporation heated by thermal conduction during magnetic reconnection at the boundary of the supergranulation cell (Wang & Sheeley 1995).

Due to the overlapping of plume structure with foreground and background and the lack of observations at higher resolution, the triggering mechanism of the polar plume is still not well understood. Together with the new opportunity with the next-generation coronagraph, the Coronal Diagnostic

Experiment, that provides the electron temperature and speed structure of plumes (Cho et al. 2017), imaging and spectroscopic observations using high-resolution telescopes from the ground (e.g., the Goode Solar Telescope at Big Bear Solar Observatory) and space (e.g., the Interface Region Imaging Spectrograph) focusing on the plumes' roots in polar coronal holes is essential to address a new model for understanding the physical mechanisms that take place in active plumes.

This work was supported the Korea Astronomy and Space Science Institute under the R&D program (2021-1-850-09). I.H.C. acknowledges support from the National Research Foundation of Korea (NRF-2019R1C1C1006033). M.M. was supported by the Brain Pool Program of the National Research Foundation of Korea (NRF-2019H1D3A2A01099143). K.S.L. was supported by the National Research Foundation of Korea (NRF-2020R1A2C2004616).

ORCID iDs

Kyung-Suk Cho  <https://orcid.org/0000-0003-2161-9606>
 Il-Hyun Cho  <https://orcid.org/0000-0001-7514-8171>
 Maria S. Madjarska  <https://orcid.org/0000-0001-9806-2485>
 Valery M. Nakariakov  <https://orcid.org/0000-0001-6423-8286>
 Heesu Yang  <https://orcid.org/0000-0001-5455-2546>
 Seonghwan Choi  <https://orcid.org/0000-0002-1946-7327>
 Eun-Kyung Lim  <https://orcid.org/0000-0002-7358-9827>
 Yeon-Han Kim  <https://orcid.org/0000-0001-5900-6237>

References

- Banerjee, D., Gupta, G. R., & Teriaca, L. 2011, *SSRv*, **158**, 267
 Banerjee, D., O'Shea, E., Doyle, J. G., et al. 2000, in AIP Conf. Proc. 537, Waves in Dusty, Solar, and Space Plasmas, ed. F. Verheest et al. (Melville, NY: AIP), 160
 Banerjee, D., O'Shea, E., & Doyle, J. G. 2000, *SoPh*, **196**, 63
 Banerjee, D., Teriaca, L., Gupta, G. R., et al. 2009, *A&A*, **499**, L29
 Brueckner, G. E., Howard, R. A., Koomen, M. J., et al. 1995, *SoPh*, **162**, 357
 Cho, I.-H., Nakariakov, V. M., Moon, Y.-J., et al. 2020, *ApJL*, **900**, L19
 Cho, K.-S., Bong, S.-C., Choi, S., et al. 2017, *JKAS*, **50**, 139
 Cho, K.-S., Yang, H., Lee, J.-O., et al. 2020, *JKAS*, **53**, 87
 Cram, L. E. 1976, *SoPh*, **48**, 3
 de Moortel, I. 2009, *SSRv*, **149**, 65
 De Moortel, I., & Nakariakov, V. M. 2012, *RSPTA*, **370**, 3193
 DeForest, C. E., & Gurman, J. B. 1998, *ApJL*, **501**, L217
 DeForest, C. E., Howard, T. A., & McComas, D. J. 2014, *ApJ*, **787**, 124
 Del Zanna, G., Bromage, B. J. I., & Mason, H. E. 2003, *A&A*, **398**, 743
 Domingo, V., Fleck, B., & Poland, A. I. 1995, *SoPh*, **162**, 1
 Golub, L., Deluca, E., Austin, G., et al. 2007, *SoPh*, **243**, 63
 Gopalswamy, N., Newmark, J., Yashiro, S., et al. 2020, *SoPh*, **296**, 15
 Gupta, G. R. 2014, *A&A*, **568**, A96
 Gupta, G. R., Banerjee, D., Teriaca, L., et al. 2010, *ApJ*, **718**, 11
 Gupta, G. R., Teriaca, L., Marsch, E., et al. 2012, *A&A*, **546**, A93
 Hanaoka, Y., Hasuo, R., Hirose, T., et al. 2018, *ApJ*, **860**, 142
 Jiao, F.-R., Xia, L.-D., Huang, Z.-H., et al. 2016, *RAA*, **16**, 93
 Kosugi, T., Matsuzaki, K., Sakao, T., et al. 2007, *SoPh*, **243**, 3
 Krishna Prasad, S., Banerjee, D., & Gupta, G. R. 2011, *A&A*, **528**, L4
 Lemen, J. R., Title, A. M., Akin, D. J., et al. 2012, *SoPh*, **275**, 17
 Madjarska, M. S. 2019, *LRSP*, **16**, 2
 McIntosh, S. W., Innes, D. E., de Pontieu, B., et al. 2010, *A&A*, **510**, L2
 Morgan, H., & Druckmüller, M. 2014, *SoPh*, **289**, 2945
 Morgan, H., Habbal, S. R., & Woo, R. 2006, *SoPh*, **236**, 263
 Nakariakov, V. M. 2006, *RSPTA*, **364**, 473
 Narukage, N., Sakao, T., Kano, R., et al. 2014, *SoPh*, **289**, 1029
 O'Dwyer, B., Del Zanna, G., Mason, H. E., et al. 2010, *A&A*, **521**, A21
 Ofman, L., Nakariakov, V. M., & DeForest, C. E. 1999, *ApJ*, **514**, 441
 Ofman, L., Romoli, M., Poletto, G., et al. 1997, *ApJL*, **491**, L111
 Pesnell, W. D., Thompson, B. J., & Chamberlin, P. C. 2012, *SoPh*, **275**, 3
 Poletto, G. 2015, *LRSP*, **12**, 7
 Pucci, S., Poletto, G., Sterling, A. C., et al. 2014, *ApJ*, **793**, 86
 Raouafi, N.-E., Petrie, G. J. D., Norton, A. A., et al. 2008, *ApJL*, **682**, L137
 Raouafi, N.-E., & Stenborg, G. 2014, *ApJ*, **787**, 118
 Reginald, N. L., Davila, J. M., St. Cyr, O. C., et al. 2017, *JGRA*, **122**, 5856
 Tian, H., McIntosh, S. W., Habbal, S. R., et al. 2011, *ApJ*, **736**, 130
 Verwichte, E., Marsh, M., Foullon, C., et al. 2010, *ApJL*, **724**, L194
 Wang, Y.-M., & Sheeley, N. R. 1995, *ApJ*, **452**, 457
 Young, P. R., Klimchuk, J. A., & Mason, H. E. 1999, *A&A*, **350**, 286
 Zangrilli, L., & Giordano, S. M. 2020, *A&A*, **643**, A104
 Zavershinskii, D. I., Kolotkov, D. Y., Nakariakov, V. M., et al. 2019, *PhPI*, **26**, 082113